Journal of Power Sources 617 (2024) 235154

Contents lists available at ScienceDirect

Journal of Power Sources

journal homepage: www.elsevier.com/locate/jpowsour

Understanding the influence of local structure distortions on Na-ion migration in perovskite solid electrolytes

Frederick P. Marlton [a], Frederick Z.T. Yang [b,1], S. Michelle Everett [c], Joerg Neuefeind [c], Siegbert Schmid [b,*]

[a] Centre for Clean Energy Technology, School of Mathematical and Physical Sciences, Faculty of Science, University of Technology Sydney, Sydney, NSW, 2007, Australia
[b] School of Chemistry, The University of Sydney, Sydney, NSW, 2006, Australia
[c] Neutron Scattering Division, Oak Ridge National Laboratory, Oak Ridge, TN, 37731, USA

HIGHLIGHTS

- Local structure of $Na_{1/2-x}La_{1/2-x}Sr_{2x}ZrO_3$ investigated via neutron total scattering.
- Small-box modelling shows local-scale features deviate from the average structure.
- Big-box modelling shows differences for bonding configurations of the A-site cations.

GRAPHICAL ABSTRACT

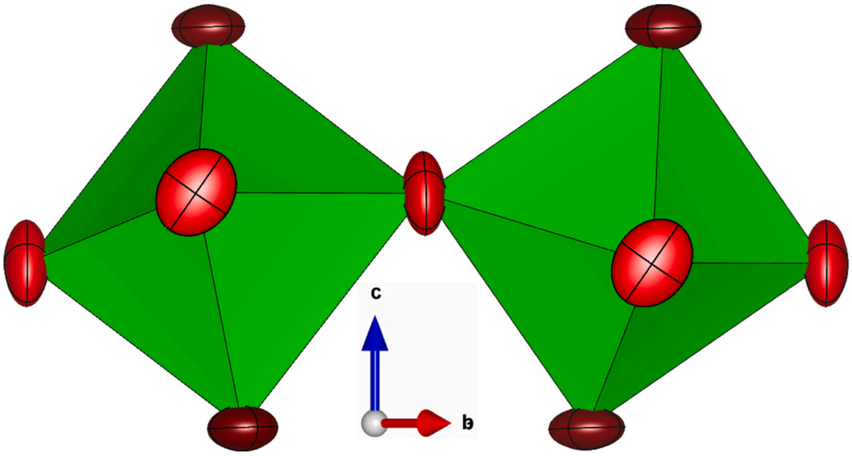

ABSTRACT

The perovskite structured oxides of composition ABO_3 are considered strong candidates for solid-state electrolytes in all-solid-state batteries due to their chemical and structural flexibility. However, further improvements must be made before they become commercially viable, and this requires a clear understanding of the structure-property relationships. In this study, the local structure of the perovskite sodium-ion solid electrolyte series $Na_{1/2-x}La_{1/2-x}Sr_{2x}ZrO_3$ (NLSZ, $x = 1/4, 1/6, 1/8, 1/16$) was investigated via neutron total scattering. Small-box modelling against the neutron pair distribution function with the orthorhombic *Pbnm* structure showed local-scale features that deviate from the average structure. Big-box modelling revealed significant differences between the bonding configurations of the different A-site cations, which impacts the ionic conductivity of the material. This study demonstrates how understanding local-scale disorder is important for tuning the structure-property relationships of inorganic solid-state electrolyte materials in sustainable battery technologies.

---

[*] Corresponding author.
E-mail address: siegbert.schmid@sydney.edu.au (S. Schmid).

[1] Present address: Chemistry research laboratory, Department of Chemistry, University of Oxford, 12 Mansfield Road, Oxford, United Kingdom.

https://doi.org/10.1016/j.jpowsour.2024.235154
Received 19 June 2024; Received in revised form 24 July 2024; Accepted 28 July 2024

1. Introduction

In the transition to a low carbon economy, sodium-ion batteries (SIBs) have attracted a lot of attention for low-cost grid-scale storage of renewable energy [1–4]. Additionally, all-solid-state batteries (ASSBs) are developing to address the major safety concerns of flammable organic based liquid electrolytes in current rechargeable battery technologies [5]. The realization of ASSBs requires solid-state electrolytes (SSEs) which exhibit high ionic conductivity, low electron conductivity, wide electrochemical window, and low interface resistance between the electrode and the solid electrolyte [6].

The common sodium-based SSEs can be categorized as inorganic, polymer or inorganic-polymer hybrids [7]. The inorganic SSEs typically have good room temperature ionic conductivity and high mechanical strength. However, they suffer drawbacks with high contact resistance between SSEs and electrodes and air sensitivity. The properties of inorganic SSEs can be improved through heteroatom doping and interface engineering [7]. Heavily investigated materials include Na β-alumina [8], Na superionic conductors (NASICONs) [9–14] and sulfides [15]. Perovskite-type materials have also been identified as potential candidates for batteries [6,16]. Perovskites are well known for their stability and flexible crystal structures, allowing for optimization of ion mobility through chemical doping. The perovskite structured lithium-ion conductor $Li_{3x}La_{2/3-x}TiO_3$ (LLTO) has shown high ionic conductivity and a relatively wide electrochemical window [17–19]. Chemical doping on the *A*- and *B*-sites influences the octahedral tilting and unit cell volume, which affect the diffusion pathway for Li^+ ions [20–23]. This LLTO system has inspired investigations on Na-based perovskite analogues, such as $Na_{1.5}La_{1.5}TeO_6$ [24], $Na_xLa_{2/3-1/3x}ZrO_3$ and $Na_xLa_{1/3-1/3x}Ba_{0.5}ZrO_3$ [25].

This study investigates the $Na_{1/2-x}La_{1/2-x}Sr_{2x}ZrO_3$ (NLSZ, $x = 1/4$, $1/6$, $1/8$, $1/16$) perovskite materials, which were shown to exhibit high ionic conductivity at room temperature for $x = 1/6$ [26]. Recent work by Yang et al. [27] showed that the long-range structure of these materials is orthorhombic *Pbnm* (Figs. S1–S3) using a combination of X-ray and neutron powder diffraction. This surpassed previous studies that indicated the long-range structure to be cubic $P2_13$,[26] demonstrating the importance of accurate structural characterization.

With advancements in materials synthesis and automation, the correct characterization of functional materials is more important than ever [28,29] to develop a complete understanding of structure-property relationships for rational materials design. Additionally, understanding the influence of structural disorder and order in compositionally complex materials provides new challenges in this area. Recent studies of perovskite structured oxides have demonstrated that chemical heterogeneity can result in local-scale distortions that are often ignored in the long-range structure [30–32].

To further understand the NLSZ materials, we investigated the local structure of the four compositions in the series using neutron pair distribution function (NPDF) analysis. The NPDF is obtained via Fourier transform of neutron total scattering data, which encompasses the long-range features from the Bragg peaks and the short-range features from the diffuse scattering. Neutrons are sensitive to both the metal and oxygen atoms in this study, providing detailed structural information that would be missed when using X-rays alone. The local structure was uncovered using small- and big-box modelling to develop a thorough understanding of the differences between the local and long-range structures [33–39].

2. Methods

Details regarding the sample synthesis are outlined in the previous publication by Yang et al. [27] Neutron scattering data were collected using the Nanoscale Ordered MAterials Diffractometer (NOMAD) [40] at the Spallation Neutron Source (SNS) located at Oak Ridge National Laboratory (ORNL). The samples were loaded into 3 mm quartz capillaries. Structural refinements against the Bragg data were conducted using the software TOPAS [41]. Resultant fits from Rietveld refinements against the Bragg data are shown in Figs. S4–S7, demonstrating single phase samples with long-range orthorhombic *Pbnm* structure. For the NPDF calculation, the neutron scattering data were corrected for instrument background, the incident neutron spectrum, absorption and multiple scattering, and finally normalized. Software available at the beamline was used to calculate the NPDF from the NOMAD data. A Q_{max} of 31.4 $Å^{-1}$ was used for the NPDF calculation. All data were collected at room temperature. The reciprocal space $S(Q)$ is shown in Fig. S8. Structural refinements against the NPDF data were conducted using the software TOPAS [41]. Partial NPDFs from the small-box modelling were calculated using RMCProfile [42]. Structure representations were drawn using VESTA [43]. Big-box modelling against the total scattering data was conducted using RMCProfile. For all compositions, starting configurations were generated from their best fit of the *Pbnm* model to the NPDF data over $1.2 - 30$ Å. Boxes were $10 \times 10 \times 7$ unit cells, containing 14 000 atomic sites and dimensions of $\sim 54 \times 54 \times 54$ $Å^3$. Fits were conducted against the NPDF over 1.90–20.0 Å and $F(Q)$ over 0.76–31.4 $Å^{-1}$. The NPDF was fit using the notation from Eq. 10 in Keen [44], as the local structure has a greater influence over the RMC fitting algorithm in this notation. This format of the NPDF was calculated using the StoG routine distributed as part of the RMCProfile package [42,45]. The Bragg data were omitted from the RMC fitting to emphasise any differences between the long and short-range structures. The weight optimization algorithm in RMCProfile was implemented with the NPDF data being weighted the highest. The bond valence sum (BVS) restraint was implemented as a soft chemical restraint to reduce unphysical bonding configurations [46]. The 'distance-window' constraint was implemented to set hard minimum and maximum nearest neighbor pair distances to prevent unphysical pair distances. Swapping between different cations occupying the same sites in the ABO_3 structure was allowed. Hence, Na, La and Sr were allowed to swap. RMC refinements were repeated 20 times to assess variation between the results and to improve statistics. For interpretation and analysis, atomic displacements were compared to those of the initial *Pbnm* structures. Atomic displacement parameters were calculated from the resultant big-box using the thermal ellipsoid tool in the RMCProfile.

3. Results and discussion

The room temperature NPDF of the four NLSZ compositions is shown in Fig. 1a and Fig. S9. Small box modelling was conducted against the NPDF data using the long-range *Pbnm* orthorhombic perovskite model with the resultant fit for $x = 1/6$ shown in Fig. 1b and remaining compositions in Figs. S10–S13. The partial PDFs for each of these fits over 1.5–4.9 Å is shown in Figs. S14–S17. Viewing the NPDF peaks between 1.5 and 4.5 Å shows the characteristic nearest neighbor peaks of the *Pbnm* perovskite structure. These peaks include Zr–O at ~2.1 Å, A–O at 2.3–3.6 Å, O–O at 2.8–3.1 Å, A–Zr at 3.4–3.6 Å, and A-A/Zr–Zr at ~4.1 Å. There are subtle differences between the NPDF of each composition, with slight broadening of the peaks at ~2.1 Å and ~2.9 Å as x decreases from $1/4$ to $1/16$. Additionally, there is a slight shift in the peak near 2.5 Å to lower r (Fig. 1a and Fig. S9), which is solely due to changes in A-O pairs. Overall, adequate small-box fits were achieved with the *Pbnm* model, but there are features that were unable to be fit well. This is most obvious for the features between 2.3 and 3.2 Å (Figs. S14–S17), corresponding to A-O and O–O pairs in the structure and most likely relates to the mixed occupancy of the A-site. Additionally, the R_{wp} is unacceptably high for a stable crystalline material at room temperature with high quality total scattering data (Figs. S4–S8). In summary, the small-box modelling demonstrates the presence of local-scale features that cannot be described with the long-range *Pbnm* structure.

To understand the structure further, big-box modelling via an RMC

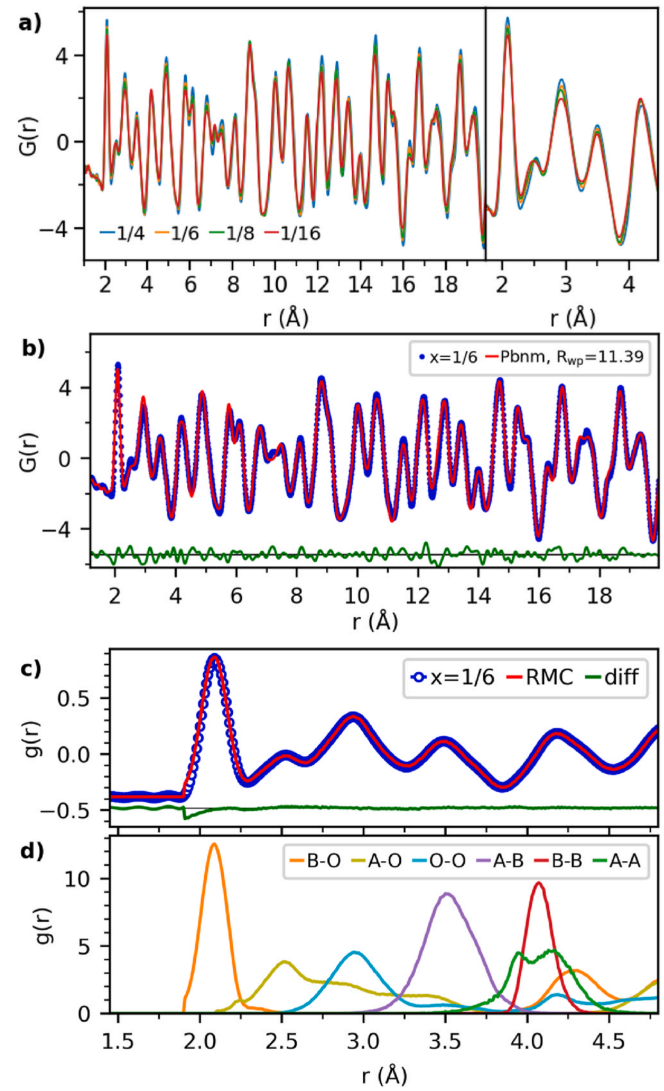

Fig. 1. a) NPDF data as a function of composition for the NLSZ series over 1.0–20.0 Å. The right panel shows the peaks corresponding to the nearest neighbor pairs over 1.75–4.45 Å. This is replicated on a larger image in Figure S9 b) Small box modelling with the orthorhombic *Pbnm* structure against the NPDF data of NLSZ with $x = 1/6$, with remaining compositions in Figs. S10–S13 c) RMC fit to the NPDF data over 1.45–4.80 Å with partialNPDFs plotted below in d). The partials shown are for the main ABO_3 perovskite sites, with more detailed partials and remaining compositions shown in Figs. S22–S25.

fit was conducted. This allowed for many more degrees of freedom to elucidate the different local configurations of the A-site cations. Example RMC fits to the NPDF data are shown in Fig. 1c and Figs. S18–S21. The partial PDFs were extracted with the simplified perovskite ABO_3 partials for $x = 1/8$ shown in Fig. 1d, and more detailed partials for all compositions shown in Figs. S22–S25. The Zr–O and Zr–Zr peaks show very little change with composition and the peaks are quite symmetrical. This demonstrates that any local scale deviations from the average structure do not arise from the Zr. The more interesting information comes from the oxygen sublattice and the A-site cations.

In the *Pbnm* model the AO_{12} polyhedron contains 8 shorter A-O bonds between 2.4 and 3.0 Å and 4 longer A-O bonds between 3.2 and 3.5 Å (Figs. S1–S3 and Figs. S14–S17). This is due to a combination of the off-center A-site (relative to a simple $Pm\overline{3}m$ cubic perovskite) and ZrO_6 octahedral tilting. Hence, the broad distribution of the A-O pairs in Fig. 1d and Figs. S22–S25 is not surprising. Histograms of the nearest neighbor A-O distances from the RMC model are shown in Fig. 2a for $x = 1/6$ and Figs. S26–S29 for the remaining compositions. This clearly shows the different A-O distribution for each A-site cation. In the case of Na, a more symmetric Na–O distribution is observed, which is very different from the La and Sr distributions, with La exhibiting the shortest O distances. Comparing these distributions to the partial PDFs from small-box modelling (Figs. S14–S17) shows that SrO_{12} shows the greatest similarity to the *Pbnm* model and LaO_{12} appears to be slightly more distorted, which could be due to increased octahedral tilting.

Observing the A-Zr distances in Fig. 2b and Figs. S26–S29 for the different A-sites shows a significantly different distribution for Na–Zr compared to La–Zr and Sr–Zr. The Na–Zr distribution is broader, indicating greater variety of Na–Zr distances and the mean Na–Zr distance is shorter. Similarly, the A-A distances (Fig. 2c and Figs. S26–S29) show the largest variation in the Na–Na distances and the smallest variation in the La–La distances. This is significantly different from the A-A distances that resulted from the small-box modelling (Figs. S14–S17), where differences between A-site cations could not be determined. Observing the bond angles (Fig. 2d and Fig. S30) shows that Na deviates from La and Sr. For La and Sr, the distribution of bond angles of the AO_{12} polyhedra closely matches the bond angles expected from an orthorhombic *Pbnm* structure, with splitting of the peaks at 60 and 120°. For the NaO_{12} polyhedron, the peaks in the distribution are significantly broadened and the intensity of the distinct *Pbnm* peaks is very different from La and Sr.

The distribution of Zr–O–Zr angles for different compositions is shown in Fig. 2e. This angle relates to the degree of octahedral tilting in the structure, with higher angles indicating less tilting. As the composition changes from $x = 1/4$ to $1/16$, the distribution becomes broader and the center shifts to lower angles, which indicates increased octahedral tilting with a lower concentration of Sr. This correlates with the results observed in Yang et al. [27] Fig. S31 shows the distribution of O–Zr–O angles across the compositional series. This angle corresponds to the internal angle in the ZrO_6 octahedra. As the composition changes from $x = 1/4$ to $1/16$, the distribution becomes broader, but is still centered at 90°. This indicates a greater degree of distortion of the ZrO_6 octahedra, which relates to the broadening of the Zr–O peak observed in the NPDF data.

The magnitudes of displacement of each element in the RMC model are displayed in Fig. 2f (A-site cations and $x = 1/6$), Figs. S26–S29 and Figs. S32–S39 (Zr and O ions). This displacement is calculated relative to the initial big-box configuration. The most interesting feature is the displacement of the A-site cations, with La showing the smallest displacement and Na showing the largest displacement. This is demonstrated by the broader distribution and the shift in the peak center. For comparison, the isometric atomic displacement parameters of the A, B and O sites calculated from the RMC model are shown in Figs. S40–S43. As the composition changes from $x = 1/4$ to $1/16$, they increase slightly for Zr and O, while the A-site shows a significant increase, with similar trends observed in Yang et al. [27] This correlates with the increased concentration of Na, which is more displaced.

This difference in the displacement of the A-site cations can be visualized by the 2D projections in Fig. 3 and Figs. S44–S46. These images correlate strongly with the magnitude of displacement shown thus far. The Na in particular has a slightly asymmetric distribution with a greater amount of displacement along the b axis. Overall, there is clear deviation of the Na away from the A-site position in the *Pbnm* structure. The distribution of the O1 (Wyckoff 4c) and O2 (Wyckoff 8d) sites can be modelled using anisotropic displacement parameters, which is illustrated in Fig. 4 for a single RMC run for $x = 1/6$. This is indicative of rotational disorder of the ZrO_6 octahedra.

The bond valence sum (BVS) of each of the ions in the structure was investigated. For the *Pbnm* model, the BVS values are shown in Table S1, while the mean and standard deviation (std) of the BVS values from the RMC model are in Tables S2 and S3, respectively. The distribution of the

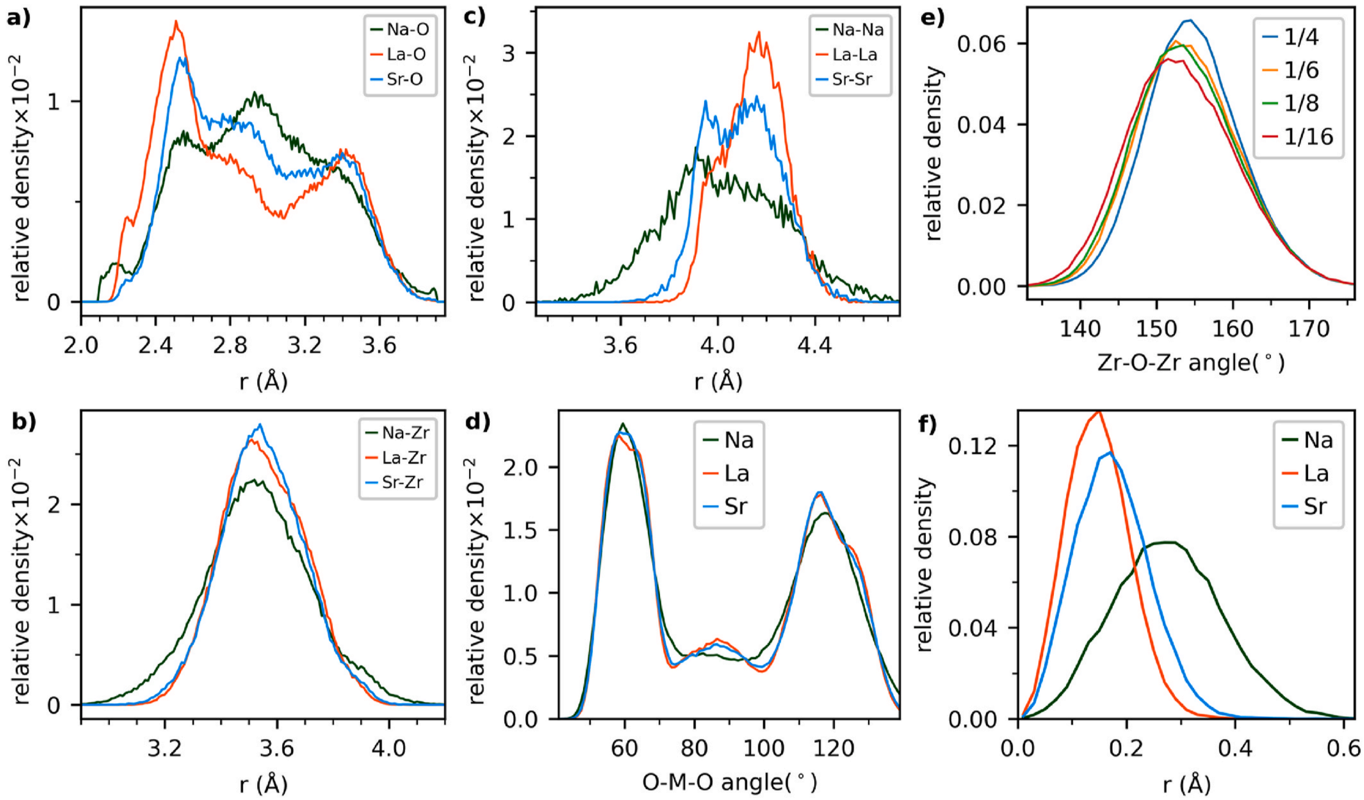

Fig. 2. (a–c) Histograms of atom-atom distances in the RMC model of NLSZ with $x = 1/6$. d,e) Histograms of the cation-oxygen bond angles in the RMC model of NLSZ with $x = 1/6$. In d), the angles correspond to those within the AO_{12} polyhedra for NLSZ with $x = 1/6$, while in e) the angle correspond to those between neighboring B-site octahedra for all NLSZ compositions in this study. f) Histograms of the magnitude of displacement of the different A-site atoms in the RMC model of NLSZ with $x = 1/6$.

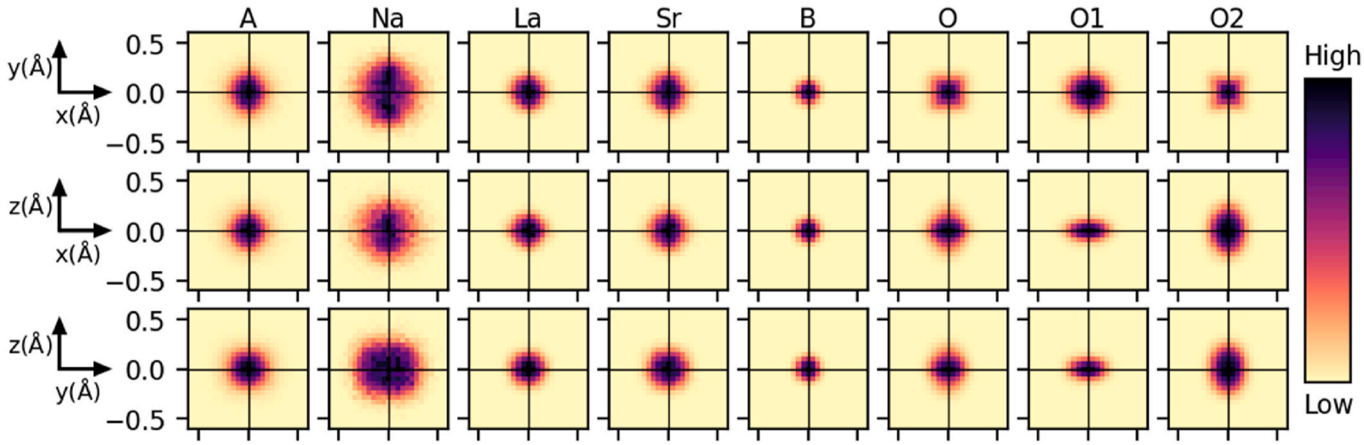

Fig. 3. Cumulative 2D probability distributions viewed down each orthogonal axis for the A, B and O sites in the RMC model of NLSZ with $x = 1/6$. The displacement of each atom is calculated relative to the initial input configuration. The A site has also been split into the constituent elements. The O site has been split into the O1 and O2 sites from the *Pbnm* model. The intensity of the color scale in each plot is normalized to itself, which means the maximum intensity between each plot is not comparable. (For interpretation of the references to color in this figure legend, the reader is referred to the Web version of this article.)

BVS values from the RMC model are shown in Figs. S47–S50. The distributions are broadest for the A-site cations and very narrow for O and Zr, which correlates with the observations thus far. In the initial configuration, the Na is slightly under bonded (BVS ≈ 0.86), but this remains the case in the final RMC model (BVS mean ≈ 0.86, BVS std ≈ 0.09), despite the large Na displacement. The oxygen is also slightly under bonded in the initial configuration, but has a mean BVS closer to 2 in the final RMC model. The Zr and Sr show no major changes between the initial and final configurations and have BVS values close to their expected valences. The La shows the largest change, with initial BVS ~2.4 and final mean BVS ~3.0. Despite this, the La is the least displaced and the Na is the most displaced in the RMC model relative to the initial configuration.

Across the compositional NLSZ series, the long-range structure at room temperature is orthorhombic *Pbnm* from $x = 0$ ($Na_{½}La_{½}ZrO_3$) to $x = 0.5$ ($SrZrO_3$) [47,48]. Assuming a 12-coordinate environment, Na^+, Sr^{2+}, and La^{3+} have ionic radii of 1.39, 1.44 and 1.36 Å, respectively [49]. Given this, the lattice volume decreases as x decreases. For the

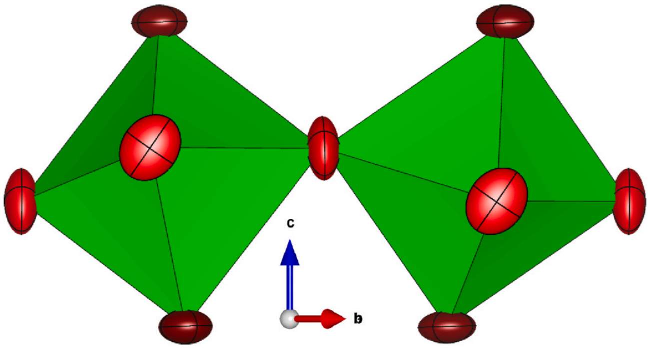

Fig. 4. Representation of the ZrO_6 octahedra from the average unit cell of the final RMC model of NLSZ with $x = 1/6$. Oxygen atoms have been drawn as red ellipsoids and the A and B sites have been omitted. The dark and light red ellipsoids correspond to the O1 (Wyckoff 4c) and O2 (Wyckoff 8d) sites in the orthorhombic *Pbnm* structure, respectively. (For interpretation of the references to color in this figure legend, the reader is referred to the Web version of this article.)

mixed compositions considered in this study, the local structures show deviations from the long-range structure due to the mixed occupancy of the A-site, with each metal ion having their own bonding preferences. This also influences the oxygen sublattice.

When considering La, there is a big shift in the BVS from ~2.4 to ~3.0, but the La does not shift from the original A-site coordinate in the *Pbnm* structure. Instead, the O atoms accommodate the La through greater degrees of octahedral rotation. This correlates with well-known perovskite chemistry, where for $ATiO_3$ (A = Ca, Sr, Ba) octahedral rotation increases for smaller A-site ionic radii. Interestingly, the BVS of the Na does not change substantially between the initial *Pbnm* and final RMC model despite the large Na displacement.

The disordered nature of the Na within the NaO_{12} polyhedra most likely influences the ionic conductivity. However, a clear trend between Na displacements and conductivity was not observed. According to Zhao et al. [26], the conductivity is highest for $x = 1/6$, while we have shown that the Na displacement increases with decreasing x. Given this, there must be a relationship between Na displacements and lattice volume that influence the conductivity. The lower values of x result in a smaller lattice and greater degrees of octahedral rotation, which could reduce the Na ion mobility. It appears that for higher concentrations of Sr (i.e. $x > 1/6$), the lattice expansion reaches a saturation point, where further expansion no longer improves the conductivity, along with decreasing the concentration of Na. Further investigation of the local structure of similar materials with different cations that influence the lattice volume is necessary to optimize these materials.

4. Conclusion

The local structure of the perovskite sodium-ion solid electrolyte series NLSZ ($x = 1/4, 1/6, 1/8, 1/16$) was investigated via neutron total scattering at room temperature. Small-box modelling unequivocally showed that the local structure of these compounds is more complex than the average structure, which is due to the mixed A-site cations. Big-box modelling was conducted to characterise the local-scale disorder. Within the AO_{12} polyhedron of the perovskite structure the Na is heavily displaced. The combination of the Na and La results in rotational disorder of the ZrO_6 octahedra and lattice contraction, while the Sr expands the lattice, which no longer has a positive impact on the conductivity for $x > 1/6$. These structural features influence the Na mobility and hence ionic conductivity. This local scale understanding of the structure provides a complete picture of the structure-property relationships that must be considered when optimising these materials through compositional modification or theoretical modelling. Through studying the local structures of these compositionally complex materials, the rational development of high-performance Na-based solid-state electrolytes can be achieved.

CRediT authorship contribution statement

Frederick P. Marlton: Writing – review & editing, Writing – original draft, Visualization, Software, Methodology, Investigation, Formal analysis, Data curation. **Frederick Z.T. Yang:** Writing – review & editing, Methodology, Investigation, Data curation, Conceptualization. **S. Michelle Everett:** Writing – review & editing, Software, Resources, Methodology, Data curation. **Joerg Neuefeind:** Writing – review & editing, Software, Resources, Methodology, Data curation. **Siegbert Schmid:** Writing – review & editing, Writing – original draft, Validation, Supervision, Resources, Project administration, Investigation, Funding acquisition, Conceptualization.

Declaration of competing interest

The authors declare that they have no known competing financial interests or personal relationships that could have appeared to influence the work reported in this paper.

Data availability

Data will be made available on request.

Acknowledgements

The Sydney based authors acknowledge and pay respect to the Gadigal people of the Eora Nation, the Traditional Owners of the land on which we research, teach and collaborate at the University of Sydney and the University of Technology Sydney. A portion of this research used resources at the SNS, a DOE Office of Science User Facility operated by ORNL. Data was collected on the NOMAD beamline (IPTS #27671.1) at the SNS, ORNL.

Appendix A. Supplementary data

Supplementary data to this article can be found online at https://doi.org/10.1016/j.jpowsour.2024.235154.

References

[1] H.S. Hirsh, et al., Sodium-ion batteries Paving the way for grid energy storage, Adv. Energy Mater. 10 (2020) 2001274, https://doi.org/10.1002/aenm.202001274.

[2] J.-Y. Hwang, S.-T. Myung, Y.-K. Sun, Sodium-ion batteries: present and future, Chem. Soc. Rev. 46 (2017) 3529–3614, https://doi.org/10.1039/c6cs00776g.

[3] N. Yabuuchi, K. Kubota, M. Dahbi, S. Komaba, Research development on sodium-ion batteries, Chem. Rev. 114 (2014) 11636–11682, https://doi.org/10.1021/cr500192f.

[4] M.D. Slater, D. Kim, E. Lee, C.S. Johnson, Sodium-ion batteries, Adv. Funct. Mater. 23 (2013) 947–958, https://doi.org/10.1002/adfm.201200691.

[5] R. Chen, Q. Li, X. Yu, L. Chen, H. Li, Approaching practically accessible solid-state batteries: stability issues related to solid electrolytes and interfaces, Chem. Rev. 120 (2020) 6820–6877, https://doi.org/10.1021/acs.chemrev.9b00268.

[6] J. Lu, Y. Li, Perovskite-type Li-ion solid electrolytes: a review, J. Mater. Sci. Mater. Electron. 32 (2021) 9736–9754, https://doi.org/10.1007/s10854-021-05699-8.

[7] Y. Dong, P. Wen, H. Shi, Y. Yu, Z.S. Wu, Solid-state electrolytes for sodium metal batteries: recent status and future opportunities, Adv. Funct. Mater. 34 (2024), https://doi.org/10.1002/adfm.202213584.

[8] M.-C. Bay, et al., Sodium plating from Na-β″-Alumina ceramics at room temperature, paving the way for fast-charging all-solid-state batteries, Adv. Energy Mater. 10 (2020) 1902899, https://doi.org/10.1002/aenm.201902899.

[9] E.A. Cheung, et al., Structure and dynamics in Mg^{2+}-stabilized γ-Na_3PO_4, J. Am. Chem. Soc. 143 (2021) 17079–17089, https://doi.org/10.1021/jacs.1c06905.

[10] E.A. Cheung, et al., Insights into the fast sodium conductor NASICON and the effects of Mg^{2+} doping on Na^+ conductivity, Chem. Mater. 33 (2021) 8768–8774, https://doi.org/10.1021/acs.chemmater.1c02846.

[11] Z. Jian, Y.S. Hu, X. Ji, W. Chen, NASICON-Structured materials for energy storage, Adv. Mater. 29 (2017) 1601925, https://doi.org/10.1002/adma.201601925.

[12] C. Shi, et al., Zero-strain $Na_3V_2(PO_4)_2F_3$@Rgo/CNT composite as a wide-temperature-tolerance cathode for Na-ion batteries with ultrahigh-rate performance, Small Methods 8 (2024) 2301277, https://doi.org/10.1002/smtd.202301277.

[13] J. He, T. Tao, F. Yang, Z. Sun, H. Huang, Phase-manipulated hierarchically core-shell $Na_3(VO_{1\text{-}x}PO_4)_2F_{1+2x}$ ($0 \leq x \leq 1$)@$Na_3V_2(PO_4)_3$ and its synergistic effect with conformally wrapped reduced graphene oxide framework towards high-performance cathode for sodium-ion batteries, Materials Today Physics 27 (2022) 100813, https://doi.org/10.1016/j.mtphys.2022.100813.

[14] J. He, T. Tao, F. Yang, Z. Sun, Manipulating the phase compositions of $Na_3(VO_{1-x}PO_4)_2F_{1+2x}$ ($0 \leq x \leq 1$) and their synergistic effects with reduced graphene oxide toward high-rate sodium-ion batteries, ACS Appl. Mater. Interfaces 13 (2021) 60099–60114, https://doi.org/10.1021/acsami.1c21271.

[15] J. Yue, et al., High-performance all-inorganic solid-state sodium–sulfur battery, ACS Nano 11 (2017) 4885–4891, https://doi.org/10.1021/acsnano.7b01445.

[16] P. Tan, M. Liu, Z. Shao, M. Ni, Recent advances in perovskite oxides as electrode materials for nonaqueous lithium–oxygen batteries, Adv. Energy Mater. 7 (2017) 1602674, https://doi.org/10.1002/aenm.201602674.

[17] Y. Sun, et al., Recent progress in lithium lanthanum titanate electrolyte towards all solid-state lithium ion secondary battery, Crit. Rev. Solid State Mater. Sci. 44 (2019) 265–282, https://doi.org/10.1080/10408436.2018.1485551.

[18] C.-h. Chen, J. Du, Lithium ion diffusion mechanism in lithium lanthanum titanate solid-state electrolytes from atomistic simulations, J. Am. Ceram. Soc. 98 (2015) 534–542, https://doi.org/10.1111/jace.13307.

[19] Y. Inaguma, et al., High ionic conductivity in lithium lanthanum titanate, Solid State Commun. 86 (1993) 689–693, https://doi.org/10.1016/0038-1098(93)90841-A.

[20] Y. Inaguma, L. Chen, M. Itoh, T. Nakamura, Candidate compounds with perovskite structure for high lithium ionic conductivity, Solid State Ionics 70–71 (1994) 196–202, https://doi.org/10.1016/0167-2738(94)90309-3.

[21] W.R. Brant, et al., Rapid lithium insertion and location of mobile lithium in the defect perovskite $Li_{0.18}Sr_{0.66}Ti_{0.5}Nb_{0.5}O_3$, ChemPhysChem 13 (2012) 2293–2296, https://doi.org/10.1002/cphc.201200017.

[22] J. Sanz, J.A. Alonso, A. Varez, M.T. Fernández-Díaz, Octahedral tilting and ordering of vacancies in the fast ion conductor $Li_{0.12}La_{0.63}TiO_3$ perovskite: a neutron diffraction study, J. Chem. Soc., Dalton Trans. 7 (2002) 1406–1408, https://doi.org/10.1039/b109926b.

[23] W.R. Brant, et al., A large format in operando wound cell for analysing the structural dynamics of lithium insertion materials, J. Power Sources 336 (2016) 279–285, https://doi.org/10.1016/j.jpowsour.2016.10.071.

[24] M. Amores, P.J. Baker, E.J. Cussen, S.A. Corr, $Na_{1.5}La_{1.5}TeO_6$: Na^+ conduction in a novel Na-rich double perovskite, Chem. Commun. 54 (2018) 10040–10043, https://doi.org/10.1039/c8cc03367f.

[25] Y.-Y. Lin, et al., Perovskite Na-ion conductors developed from analogous $Li_{3x}La_{2/3-x}TiO_3$ (LLTO): chemo-mechanical and defect engineering, J. Mater. Chem. A 9 (2021) 21241–21258, https://doi.org/10.1039/D1TA04252A.

[26] Y. Zhao, et al., Synthesis and characterization of a new perovskite-type solid-state electrolyte of $Na_{1/3}La_{1/3}Sr_{1/3}ZrO_3$ for all-solid-state sodium-ion batteries, J. Alloys Compd. 783 (2019) 219–225, https://doi.org/10.1016/j.jallcom.2018.12.289.

[27] F.Z.T. Yang, V.K. Peterson, S. Schmid, Composition and temperature dependent structural investigation of the perovskite-type sodium-ion solid electrolyte series $Na_{1/2-x}La_{1/2-x}Sr_{2x}ZrO_3$, J. Alloys Compd. 863 (2021) 158500, https://doi.org/10.1016/j.jallcom.2020.158500.

[28] A.K. Cheetham, R. Seshadri, Artificial intelligence driving materials discovery? Perspective on the article: scaling deep learning for materials discovery, Chem. Mater. 36 (2024) 3490–3495, https://doi.org/10.1021/acs.chemmater.4c00643.

[29] J. Leeman, et al., Challenges in high-throughput inorganic materials prediction and autonomous synthesis, PRX Energy 3 (2024), https://doi.org/10.1103/prxenergy.3.011002.

[30] A. Kumar, et al., Atomic-resolution electron microscopy of nanoscale local structure in lead-based relaxor ferroelectrics, Nat. Mater. 20 (2021) 62–67, https://doi.org/10.1038/s41563-020-0794-5.

[31] F. Li, et al., Giant piezoelectricity of Sm-doped $Pb(Mg_{1/3}Nb_{2/3})O_3$-$PbTiO_3$ single crystals, Science 364 (2019) 264–268, https://doi.org/10.1126/science.aaw2781.

[32] D.S. Keeble, et al., Bifurcated polarization rotation in bismuth-based piezoelectrics, Adv. Funct. Mater. 23 (2013) 185–190, https://doi.org/10.1002/adfm.201201564.

[33] D. Hou, C. Zhao, A.R. Paterson, S. Li, J.L. Jones, Local structures of perovskite dielectrics and ferroelectrics via pair distribution function analyses, J. Eur. Ceram. Soc. 38 (2018) 971–987, https://doi.org/10.1016/j.jeurceramsoc.2017.12.003.

[34] P. Juhas, C.L. Farrow, X. Yang, K.R. Knox, S.J.L. Billinge, Complex modeling: a strategy and software program for combining multiple information sources to solve ill posed structure and nanostructure inverse problems, Acta Crystallogr. A 71 (2015) 562–568, https://doi.org/10.1107/S2053273315014473.

[35] R.L. McGreevy, Reverse Monte Carlo modelling, J. Phys. Condens. Matter 13 (2001) R877.

[36] F.P. Marlton, et al., Lattice disorder and oxygen migration pathways in pyrochlore and defect-fluorite oxides, Chem. Mater. 33 (2021) 1407–1415, https://doi.org/10.1021/acs.chemmater.0c04515.

[37] F.P. Marlton, et al., Broad distribution of local polar states generates large electrothermal properties in Pb-free relaxor ferroelectrics, Chem. Mater. 33 (2021) 8844–8853, https://doi.org/10.1021/acs.chemmater.1c03066.

[38] H. Playford, D. Keen, M. Tucker, Local structure of crystalline and amorphous materials using reverse Monte Carlo methods, Neutron News 27 (2016) 17–21, https://doi.org/10.1080/10448632.2016.1197589.

[39] S.J.L. Billinge, The rise of the X-ray atomic pair distribution function method: a series of fortunate events, Phil. Trans. Math. Phys. Eng. Sci. 377 (2019) 20180413, https://doi.org/10.1098/rsta.2018.0413.

[40] J. Neuefeind, M. Feygenson, J. Carruth, R. Hoffmann, K.K. Chipley, The nanoscale ordered MAterials diffractometer NOMAD at the spallation neutron Source SNS, Nucl. Instrum. Methods Phys. Res. Sect. B Beam Interact. Mater. Atoms 287 (2012) 68–75, https://doi.org/10.1016/j.nimb.2012.05.037.

[41] A. Coelho, TOPAS-Academic: an optimization program integrating computer algebra and crystallographic objects written in C++, J. Appl. Crystallogr. 51 (2018) 210–218, https://doi.org/10.1107/S1600576718000183.

[42] M.G. Tucker, D.A. Keen, M.T. Dove, A.L. Goodwin, Hui, Q. Rmcprofile, Reverse Monte Carlo for polycrystalline materials, J. Phys. Condens. Matter 19 (2007) 335218.

[43] K. Momma, F. Izumi, VESTA 3 for three-dimensional visualization of crystal, volumetric and morphology data, J. Appl. Crystallogr. 44 (2011) 1272–1276, https://doi.org/10.1107/S0021889811038970.

[44] D.A. Keen, A comparison of various commonly used correlation functions for describing total scattering, J. Appl. Crystallogr. 34 (2001) 172–177, https://doi.org/10.1107/S0021889800019993.

[45] Y. Zhang, M. Eremenko, V. Krayzman, M.G. Tucker, I. Levin, New capabilities for enhancement of RMCProfile: instrumental profiles with arbitrary peak shapes for structural refinements using the reverse Monte Carlo method, J. Appl. Crystallogr. 53 (2020) 1509–1518, https://doi.org/10.1107/S1600576720013254.

[46] S.T. Norberg, M.G. Tucker, S. Hull, Bond valence sum: a new soft chemical constraint for RMCProfile, J. Appl. Crystallogr. 42 (2009) 179–184, https://doi.org/10.1107/S0021889809004981.

[47] B.J. Kennedy, C.J. Howard, B.C. Chakoumakos, High-temperature phase transitions in $SrZrO_3$, Phys. Rev. B 59 (1999) 4023–4027, https://doi.org/10.1103/physrevb.59.4023.

[48] M.C. Knapp, P.M. Woodward, A-site cation ordering in $AA'BB'O_6$ perovskites, J. Solid State Chem. 179 (2006) 1076–1085, https://doi.org/10.1016/j.jssc.2006.01.005.

[49] R. Shannon, Revised effective ionic radii and systematic studies of interatomic distances in halides and chalcogenides, Acta Crystallogr. A 32 (1976) 751–767, https://doi.org/10.1107/S0567739476001551.